Article

Structural Properties and Oxidation Resistance of ZrN/SiN$_x$, CrN/SiN$_x$ and AlN/SiN$_x$ Multilayered Films Deposited by Magnetron Sputtering Technique

Ihar Saladukhin [1], Gregory Abadias [2,*], Vladimir Uglov [1,3], Sergey Zlotski [1], Arno Janse van Vuuren [4] and Jacques Herman O'Connell [4]

[1]   Faculty of Physics, Belarusian State University, 220030 Minsk, Belarus; solodukhin@bsu.by (I.S.); Uglov@bsu.by (V.U.); Zlotski@bsu.by (S.Z.)
[2]   Institut Pprime, Université de Poitiers-CNRS-ENSMA, TSA 41123, CEDEX 9, 86073 Poitiers, France
[3]   South Ural State University, 454080 Chelyabinsk, Russia
[4]   Centre for HRTEM, Nelson Mandela Metropolitan University, Port Elizabeth 6001, South Africa; arnojvv@gmail.com (A.J.v.V.); joconnell@mandela.ac.za (J.H.O.)
*   Correspondence: gregory.abadias@univ-poitiers.fr; Tel.: +33-(0)549-496-748

check for updates

Abstract: In the present work, the structure, stress state and phase composition of MeN/SiN$_x$ (Me = Zr, Cr, Al) multilayered films with the thickness of elementary layers in nanoscale range, as well as their stability to high temperature oxidation, were studied. Monolithic (reference) and multilayered films were deposited on Si substrates at the temperatures of 300 °C (ZrN/SiN$_x$ and AlN/SiN$_x$ systems) or 450 °C (CrN/SiN$_x$) by reactive magnetron sputtering. The thickness ratios of MeN to SiN$_x$ were 5 nm/2 nm, 5 nm/5 nm, 5 nm/10 nm and 2 nm/5 nm. Transmission electron microscopy (TEM), X-ray Reflectivity (XRR) and X-ray Diffraction (XRD) testified to the uniform alternation of MeN and SiN$_x$ layers with sharp interlayer boundaries. It was observed that MeN sublayers have a nanocrystalline structure with (001) preferred orientation at 5 nm, but are X-ray amorphous at 2 nm, while SiN$_x$ sublayers are always X-ray amorphous. The stability of the coatings to oxidation was investigated by in situ XRD analysis (at the temperature range of 400–950 °C) along with the methods of wavelength-dispersive X-ray spectroscopy (WDS) and scanning electron microscopy (SEM) after air annealing procedure. Reference ZrN and CrN films started to oxidize at the temperatures of 550 and 700 °C, respectively, while the AlN reference film was thermally stable up to 950 °C. Compared to reference monolithic films, MeN/SiN$_x$ multilayers have an improved oxidation resistance (onset of oxidation is shifted by more than 200 °C), and the performance is enhanced with increasing fraction of SiN$_x$ layer thickness. Overall, CrN/SiN$_x$ and AlN/SiN$_x$ multilayered films are characterized by noticeably higher resistance to oxidation as compared to ZrN/SiN$_x$ multilayers, the best performance being obtained for CrN/SiN$_x$ and AlN/SiN$_x$ with 5 nm/5 nm and 5 nm/10 nm periods, which remain stable at least up to 950 °C.

Keywords: multilayered film; metal nitride; silicon nitride; oxidation

1. Introduction

In accordance with the tendency of industry development, the coatings applied for protection of materials should satisfy more stringent requirements. They have to possess high hardness and wear resistance (e.g., pieces under friction), resistance to high temperature oxidation (e.g., cutting tools) and thermal cyclability (e.g. glass molding dies), stability in corrosive media (e.g., in chemical production units), radiation stability (e.g., materials for nuclear power engineering) and other properties. Currently, physically-vapor deposited transition metal nitride (TMN) coatings based on MeN mononitrides of transition metal (Me = Ti, Zr or Cr) are widely used [1–3]. However, mononitride films often lose

their protective role in such severe conditions. For example, TiN and ZrN coatings deposited by reactive magnetron sputtering are intensively oxidized at the temperatures of 500–600 °C [4–7]. This is related to their columnar microstructure and presence of defects (e.g., porosity or micro-cracks), which allows a direct contact between the external atmosphere and substrate and accelerates oxygen incorporation through grain boundary diffusion. Several routes can be employed to enhance oxidation resistance of MeN coatings. Musil et al. [8–10] showed that superior thermal stability, above 1000 °C, was achieved for hard amorphous coatings, based on either ternary Me-Si-N systems with Si content ≥ 20 at.% or quaternary Si-B-C-N system with covalent bonding. These amorphous coatings are generally obtained by co-sputtering method and their improved oxidation resistance is ascribed to the absence of grain boundaries.

An alternate route to nanocomposite/amorphous Me-Si-N single-layer coatings is to deposit sequentially different MeN_x layers, resulting in the formation of periodic multilayers or nanolaminates with improved performance characteristics [11]. By alternation at the nanoscale of dissimilar layers, it is possible to combine the advantages of the different materials properties, and even to get superior properties compared to monolithic films such as improved adhesion, increase in corrosion resistance or change in electrical behavior. The authors of [12] showed that, unlike CrN and AlN films, for which the generation and motion of classical dislocations is responsible for the plastic flow, the observed plastic deformation in CrN/AlN multilayered coatings is mostly governed by grain rotation for the nanocrystals and grain boundary sliding for grains of larger size. Such non-elastic phenomena prevent the deformation or crack formation that allows using CrN/AlN multilayered coatings for ductile steel substrate as well. Another example is the case of AlCrN/TiVN multilayered coatings, where the AlCrN layer inhibited the excessive oxygen diffusion into the multilayered film [13]. Consequently, it was possible to avoid rapid oxidation of vanadium and obtain high wear-resistance for the AlCrN/TiVN coating. Although the TiVN coating had the lowest friction coefficient, the lowest wear rate (1.9×10^{-7} mm^3/Nm) was obtained for the AlCrN/TiVN coated sample.

It is possible to classify three main types of multilayers based on the type of structure of the elementary layers: (i) nanocrystalline/nanocrystalline layers; (ii) nanocrystalline/amorphous layers; and (iii) amorphous/amorphous layers.

Multilayers based on TMN usually belong to the first category [12–17]. The comparison of hardness and other mechanical characteristics of multilayered coatings made of alternate stacking of various TMN is given in [15]. It is pointed that the TiN/VN multilayered coatings are one of the most successful examples of superhard materials. The maximum hardness value of these coatings reached 56 GPa (at bilayer thickness about 5.2 nm). The use of a combination of nanocrystalline/nanocrystalline layers is rather effective for achievement of high resistance of the coatings to high temperature oxidation [16,17]. High thermal stability of AlCrN/TiSiN coating is noted, for which the excellent oxidation resistance was obtained with no pore and delamination up to 900 °C [17]. In this case, the redistribution of elements between the layers takes place when forming the oxide layer, namely mixed (Al,Ti)-oxide scale outside layer and a dense $(Al,Cr)_2O_3$ inner layer.

The second group of multilayered coatings, consisting of sequentially alternating layers of nanocrystalline and amorphous material, is perspective due to the possibility of combining of the different properties. For example, the hardness and wear resistance of nanocrystalline layer are supplemented with plasticity and chemical inertness of the amorphous layer. MeN/SiN_x coatings are among the most appealing nanocrystalline/amorphous layered systems [18–21]. The characteristic feature of these films is the immiscibility of their constitutive layers at the origin of their good thermal stability and properties [20,22,23]. The enhanced stability of MeN/SiN_x films to oxidation is also related to the fact that the columnar growth of MeN layer is suppressed by the presence of the SiN_x amorphous layer [21]. This prevents from oxygen penetration deep into the film along the grain boundaries and pores concomitant to the formation of the columnar structure.

A significant increase in hardness of the MeN/SiN_x multilayered films has been reported when decreasing the thickness of SiN_x layer below ~0.8 nm [23–25]. In this case, the epitaxial growth

of silicon nitride at the interface of cubic MeN layer results in SiN_x layer crystallization. Such an effect is more pronounced for TiN/SiN_x and ZrN/SiN_x systems [18,24–26], and is less marked for the AlN/SiN_x system because the interfaces between AlN and epitaxial Si_3N_4 only slightly affect the propagation of dislocations. As the result, only a minor hardness enhancement is expected in AlN/SiN_x multilayers [27]. However, it should be noted that an increase in microhardness of MeN/SiN_x multilayered coatings at the thicknesses of SiN_x elementary layer of 1 nm and less is accompanied by a decrease in film oxidation resistance [6]. This indicates that, by controlling the ratio of individual layers, it is possible to ensure one or another required property.

Among the coatings of the third group (amorphous/amorphous layers), the coatings with alternating layers of so-called metallic glasses are of more interest for practical applications. ZrCu/ZrCuNiAlSi films are an example of radiation-resistant multilayered systems for applications in the area of materials design for nuclear power engineering [28].

In our prior work on the ZrN/SiN_x system, we showed that the coatings which belong to the second group are quite promising for use as resistant coatings under high-temperature oxidation up to 860–950 °C [6]. It should be noted that, for the CrN/SiN_x system and, especially, for the AlN/SiN_x system, the chemical inertness of SiN_x amorphous layer is supplemented by the formation of the passivating layers of metal oxide in the surface layer of the MeN/SiN_x multilayered film [17,29]. However, it is difficult to compare the oxidation behavior of the different MeN/SiN_x multilayered systems because of the different physical vapor deposition processes used for their fabrication, as well as variations in the bilayer thickness range studied. In the present work, we performed a systematic and comparative study of the structure and stability to high-temperature oxidation of ZrN/SiN_x, CrN/SiN_x and AlN/SiN_x films sputter-deposited in the same chamber, with special emphasis laid on the influence of the thickness ratio of the elementary layers. As shown previously for the ZrN/SiN_x system, the ratio of thicknesses of individual layers plays a key role in their oxidation resistance [6]. The properties of the multilayers are also discussed and compared to those of reference monolithic films.

2. Materials and Methods

Reference ZrN, CrN, AlN and Si_3N_4 monolithic films as well as ZrN/SiN_x, CrN/SiN_x and AlN/SiN_x multilayered films were grown by reactive magnetron sputter-deposition in a high vacuum chamber (base pressure $< 10^{-5}$ Pa) equipped with confocal targets configuration and a cryogenic pump (max. 500 L/s) [30]. All films were deposited on Si substrates covered with 10 nm thick thermally grown SiO_2 layer (to prevent the interdiffusion of the coating and substrate components). A constant bias voltage of -60 V was applied to the substrate during deposition. The substrate was rotated at 15 rpm throughout the deposition to ensure an equal deposition rate across the substrate surface.

Water-cooled, 7.62-cm-diameter Zr (99.2% purity), Cr (99.95% purity), Al (99.9995% purity) and Si_3N_4 (99.99% purity) targets, located at 18 cm from the substrate holder, were used under Ar + N_2 plasma discharges at constant power mode. The Zr, Cr and Al targets were operated in magnetically unbalanced configuration using a DC power supply, while for the Si_3N_4 target a RF power supply was used in balanced mode. The total working pressure varied from 0.22–0.29 Pa depending on the material system, as measured using a Baratron® capacitance gauge (Andover, MA, USA). The Ar/N_2 flow ratio was optimized to obtain stoichiometric nitrogen content in the films based on earlier results [31,32] (see Table 1). The N_2 partial pressure was measured during deposition using a MKS Microvision mass spectrometer (Munich, Germany).

The deposition conditions were not identical for all MeN layers. They varied (N_2 partial pressure and substrate temperature) to achieve the desired phase and optimal crystallinity for each MeN layer. Reference ZrN, AlN and Si_3N_4 films as well as ZrN/SiN_x and AlN/SiN_x multilayered films were deposited at 300 °C, while reference CrN film and CrN/SiN_x multilayered films were formed at the substrate temperature of 450 °C. This temperature was chosen to obtain single-phase cubic CrN phase without formation of hexagonal Cr_2N phase. The periodic growth of the multilayered systems was

monitored by computer-controlled pneumatic shutters located at 2 cm in front of each target. Details of the multilayered films growth procedure are given in [23].

Table 1. Process parameters and chemical analysis for ZrN, CrN, AlN and Si_3N_4 reference films.

Film	$T_{dep.}$ (°C)	Me Power (W)	Si_3N_4 Power (W)	Ar/N_2 Flow	Total Pressure(Pa)	Partial Pressure P_{N_2} (Pa)	Growth Rate(nm/min)	Film Thick-ness (nm)	Me (at. %)	Si (at. %)	N (at. %)
ZrN	300	300	–	10/0.5	0.22	4.6×10^{-3}	12.5	249	46.6	–	53.4
CrN	450	200	–	25/20	0.29	6.3×10^{-2}	5.4	259	54.6	–	45.4
AlN	300	300	–	24/6.5	0.22	2.4×10^{-2}	5.9	293	43.6	–	56.4
Si_3N_4	300	–	176	24/5.1	0.22	2.2×10^{-2}	2.1	287	–	43.3	56.7

Note. For ZrN/SiN_x, CrN/SiN_x and AlN/SiN_x films, the same deposition regimes as for ZrN, CrN, AlN and Si_3N_4 reference films were used.

The deposition conditions are summarized in Table 1 for the reference monolithic films, and the same conditions were used for elementary layers of the MeN/SiN_x (Me = Zr, Cr, Al) multilayers, except the deposition time. The deposition rates were 12.5, 5.9 and 5.4 nm/min for ZrN, AlN and CrN monolithic films, respectively. The use of a RF discharge to deposit the Si_3N_4 reference film resulted in a slower deposition rate of 2.1 nm/min. For mononitrides, the deposition time was adjusted between 22 min and 2.3 h to get similar nominal film thickness of ~300 nm. For MeN/SiN_x multilayers, the deposition time of constitutive sublayers was adjusted accordingly to get the desired modulation period, but the total film thickness was similar (~300 nm). For example, for MeN (5 nm)/SiNx (5 nm), the deposition times were 23 s/141 s, 50 s/141 s and 50 s/141 s for MeN=ZrN, AlN and CrN, respectively. The nominal ratios of thickness of MeN layer to SiN_x layer were 5 nm/2 nm, 5 nm/5 nm, 5 nm/10 nm and 2 nm/5 nm (see Table 2). For multilayers, the deposition process always started with the MeN sublayer being deposited first.

Table 2. Best-fit parameters as determined from simulations of XRR experimental data of MeN/SiN_x (Me = Zr, Cr, Al) multilayers: elementary layer thickness (h_{MeN} and h_{SiNx}), mass density (ρ_{MeN} and ρ_{SiNx}), interface roughness (w_{MeN} and w_{SiNx}), MeN layer fraction (f_{MeN}) and total film thickness. The first row indicates nominal thicknesses ratio for MeN/SiN_x multilayers.

Multi-Layers	MeN (Me = Zr, Cr, Al) Sublayer			SiN_x Sublayer			f_{MeN}	Number of Bilayers	Total Thickness (nm)
	h_{MeN} (nm)	ρ_{MeN} (g cm^{-3})	w_{MeN} (nm)	h_{SiNx} (nm)	ρ_{SiNx} (g cm^{-3})	w_{SiNx} (nm)			
				ZrN/SiN$_x$					
5 nm/5 nm	3.7	7.3	0.4	5.3	3.1	0.6	0.41	29	261
5 nm/10 nm	4.9	7.4	0.7	9.9	2.9	0.5	0.33	20	296
2 nm/5 nm	1.6	7.4	0.6	5.0	3.0	0.6	0.24	43	284
				CrN/SiN$_x$					
5 nm/5 nm	4.5	6.2	0.6	4.9	3.0	0.3	0.48	30	282
5 nm/10 nm	4.4	6.4	0.4	9.7	3.0	0.3	0.31	20	282
2 nm/5 nm	1.6	6.2	0.3	5.1	3.0	0.3	0.24	43	288
				AlN/SiN$_x$					
5 nm/5 nm	4.3	3.2	0.2	5.6	3.0	0.8	0.43	30	297
5 nm/10 nm	3.8	3.3	< 0.1	11.3	3.0	0.4	0.25	20	302
2 nm/5 nm	1.6	3.2	0.2	5.6	3.0	0.8	0.22	43	310

The evolution of intrinsic stress developed during growth was monitored in situ and in real-time using the wafer curvature technique [33]. A multiple-beam optical stress sensor (MOSS) designed by kSpace Associates (kSA, Dexter, MI, USA) was implemented in the deposition chamber. The measurements were performed using 150 ± 2 μm thick Si substrate covered with native oxide, under stationary mode.

High resolution transmission electron microscopy (HRTEM, JEOL JEM ARM200F, Tokyo, Japan) analysis was carried out for direct information about the film structure and state of interlayer boundaries. Cross-sectional TEM specimens were prepared using a FEI Helios Nanolab 650 focused ion beam (FIB) (Brno, Czech Republic). More details on the sample preparation can be found in [6]. All specimens

were analyzed using a JEOL JEM 2100 LaB$_6$ transmission electron microscope (Tokyo, Japan) operating at 200 kV.

The characterization of the multilayer stacking was carried out using low-angle X-ray Reflectivity (XRR). A fitting procedure, based on the optical formalism of Parratt [34], was used to extract the relevant quantities (individual layer thickness, mass density and interface roughness). The fraction of MeN (Me = Zr, Cr, Al) layer is defined as $f_{MeN} = \frac{h_{MeN}}{h_{MeN}+h_{SiN_x}}$, where h_{MeN} and h_{SiN_x} are the MeN and SiN$_x$ layer thicknesses, respectively.

The elemental composition of films in their as-deposited (for the reference films only) and air-annealed states was determined using elemental probe microanalysis. A wavelength dispersive spectrometer (WDS) unit from Oxford Instruments (High Wycombe, UK) attached to a JEOL 7001 TTLS scanning electron microscope (Tokyo, Japan) operated at 10 kV and 10 nA was used for the quantification with a precision better than 1 at.%. The same microscope was applied for obtaining top-view SEM micrographs of the films after air annealing at 950 °C.

X-ray Diffraction (XRD) analysis was employed for structural identification using a Bruker D8 AXS X-ray diffractometer (Karlsruhe, Germany) operating in Bragg–Brentano configuration and equipped with Cu$_{K_\alpha}$ wavelength (0.15418 nm) and LynxEye detector.

Isothermal air annealing was performed at different sequential temperatures from 400 to 950 °C. The oxidation process was investigated using in situ XRD experiments. The samples were placed on a resistive heating stage designed by Anton Paar (Graz, Austria) implemented on the Bruker D8 diffractometer, consisting in an AlN sample holder and a hemispheric graphite dome subjected to air blowing. Total scan time during isothermal annealing was 50–60 min.

3. Results and Discussion

3.1. Structure and Phase Composition of As-Deposited MeN/SiN$_x$ (Me = Zr, Cr, Al) Multilayered Films

As described in Section 2, the ZrN/SiN$_x$, CrN/SiN$_x$ and AlN/SiN$_x$ multilayered films with different thickness ratio of MeN (Me = Zr, Cr, Al) and SiN$_x$ elementary layers were formed. This corresponds to different MeN fractions, f_{MeN}. The elemental composition of the reference monolithic films, obtained from WDS, is given in Table 1. MeN$_x$ films are slightly off-stoichiometric: overstoichiometric ZrN$_{1.15}$ and AlN$_{1.30}$ films and substoichiometric CrN$_{0.83}$ films were obtained. However, the SiN$_x$ film has the Si$_3$N$_4$ stoichiometry.

Figure 1 shows the HRTEM images of MeN/SiN$_x$ (Me = Zr, Cr, Al) multilayered films with the ratio of elementary layer thicknesses equal to 5 nm/5 nm. It reveals the uniform alternation of MeN and SiN$_x$ elementary layers, and the formation of sharp and smooth interfaces between the layers points to the absence of intermixing of the layer components. However, the interlayer boundary seems more diffuse for the CrN/SiN$_x$ multilayer, possibly due to the growth at higher substrate temperature. While the MeN$_x$ layers appear crystalline (see, e.g., lattice fringes in AlN layer of Figure 1c), the SiN$_x$ layers were found to be amorphous. Note also a change in electronic contrast from ZrN/SiN$_x$ to AlN/SiN$_x$ multilayers, due to reduction in mass density difference between MeN and SiN$_x$ layers. The values of mass densities for the elementary layers are presented in Table 2, as extracted from the fit of XRR data (see below). In particular, the contrast between AlN and SiN$_x$ layers is very similar, as also observed by other authors [27].

Figure 2 shows the low-angle XRR scans together with the simulated curves obtained for MeN/SiN$_x$ (Me = Zr, Cr, Al) multilayered films with the nominal MeN thickness h_{MeN} = 5 nm and SiN$_x$ thickness h_{SiN_x} = 5 nm. For all multilayered systems, relatively sharp superlattice reflections are observed up to high 2θ angles (up to seventh order or more). This testifies the formation of highly periodic multilayer structures and gives evidence of the presence of relatively smooth interface boundaries between the layers. Similar results were obtained for CrN/Si$_3$N$_4$ multilayered films in [20], where the effectiveness of Si$_3$N$_4$ layer for stabilization of periodic structure was mentioned. Note that Kiessig fringes are also

distinguishable between main superlattice reflections in XRR scans (however, not visible in the scale displayed in Figure 2).
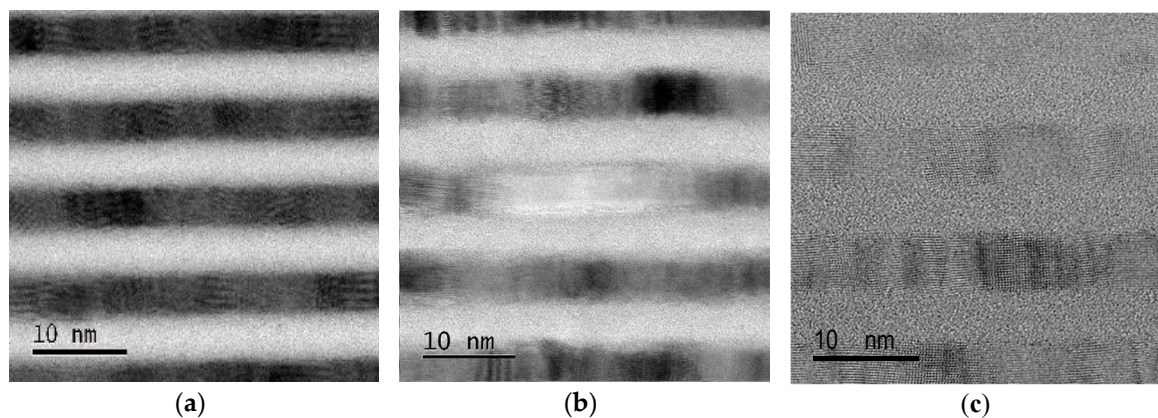

Figure 1. Cross-sectional (bright field) HRTEM images of multilayered films with the ratio of thicknesses of MeN (darker contrast) and SiN_x (brighter contrast) elementary layers equal to 5 nm/5 nm: ZrN/SiN_x (**a**); CrN/SiN_x (**b**); and AlN/SiN_x (**c**).
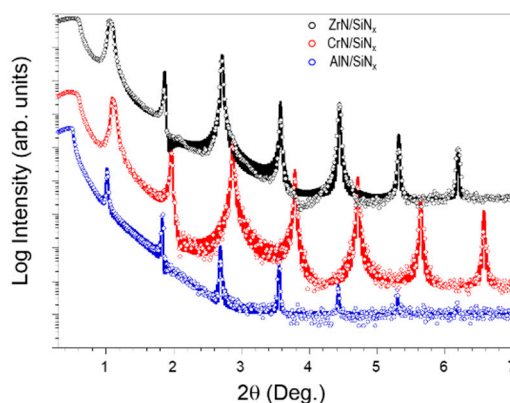

Figure 2. XRR scans of ZrN/SiN_x, CrN/SiN_x and AlN/SiN_x multilayered films with the ratio of thicknesses of MeN and SiN_x elementary layers equal to 5 nm/5 nm. Solid lines correspond to the best-fit simulations to experimental data using optical model of Parratt.

An optical simulation model was used to fit XRR data and get information on layer density, layer thickness and interface roughness of each sublayer for ZrN/SiN_x, CrN/SiN_x and AlN/SiN_x multilayers. Values are reported in Table 2 for the different systems and bilayer periods investigated. The obtained results show that the boundaries between the layers for all multilayered systems are quite smooth (the interface roughness w_{MeN} does not exceed 0.6 nm), which is in good agreement with the HRTEM observations presented in Figure 1. All MeN_x sublayers were found to be dense, with mass density of $\rho_{ZrN} = 7.4 \pm 0.1$ g·cm^{-3}, $\rho_{CrN} = 6.3 \pm 0.1$ g·cm^{-3} and $\rho_{AlN} = 3.2 \pm 0.1$ g·cm^{-3}. These values are very close to the values for bulk reference powders, being $\rho_{ZrN} = 7.29$ g·cm^{-3}, $\rho_{CrN} = 6.18$ g·cm^{-3} and $\rho_{AlN} = 3.26$ g·cm^{-3}. The value ρ_{SiNx} was found to be equal to 3.0 g· $\pm$ 0.1 cm^{-3}, also in good agreement with the bulk value of α-Si_3N_4 crystalline phase (3.18 g·cm^{-3}).

One can note from the results in Table 2 that for all multilayered films the thickness of MeN (Me = Zr, Cr, Al) layer is less than the nominal thickness. For example, for the case of nominal ratio of MeN and SiN_x thicknesses 2 nm/5 nm, the real thickness of MeN layer is 1.6 nm, i.e. 20% less. This is related to the poisoning of the metal target during the first seconds of the reactive sputter-deposition process. Consequently, the initial deposition rate is lower than the average value calculated from the

thicker reference MeN films. More information on this poisoning effect can be found in [23]. At the same time, the thickness of SiN_x layer is close to nominal one for all multilayered systems (Table 2).

Figure 3 shows the substrate curvature change measured by MOSS during growth of ZrN/SiN_x, CrN/SiN_x and AlN/SiN_x multilayered films with nominal thickness ratio 10 nm/5 nm. One can see from the slope of F/w vs. layer thickness that both sublayers develop compressive stress. However, the magnitude of the compressive stress is much larger for MeN layers than for SiN_x layers. Relatively large values of -7.2 and -5.7 GPa were obtained for the incremental stress during deposition of AlN and ZrN layers, respectively, while for CrN layers the incremental stress is -2.7 GPa. Comparatively, the incremental stress of SiN_x layer is about -1.2 GPa. One can also notice from the results in Figure 3 that the stress state is reproducible from one bilayer to another, i.e., there is no influence of the underneath layers on the cumulative stress build-up. The formation of compressive stress in sputter-deposited TMN layers is due to energetic bombardment during growth, which creates point defects in the crystal lattice and densify the grain boundaries [23,35–37]. At low deposited energy, sputter-deposited MeN_x films develop a columnar, underdense microstructure, often accompanied by the development of tensile stress [35,37,38]. This is obviously not the case here for these nanoscale layer thicknesses, because the presence of amorphous SiN_x layers interrupts the columnar growth of MeN layers. If the energy delivered to growing film is large, a dense and sometimes featureless microstructure is formed together with compressive stress. In our deposition conditions, the main contribution to the deposited energy stems from energetic neutrals (sputtered atoms and backscattered Ar) due to low fraction of bombarding ions (a few percent) reaching the substrate. The lower compressive stress values for CrN layers is likely due to the higher substrate temperature (450 °C vs. 300 °C), which favors defect annihilation processes. Amorphous layers are more tolerant to defect incorporation compared to their crystalline counterpart, which explains the lower stress values obtained for SiN_x.
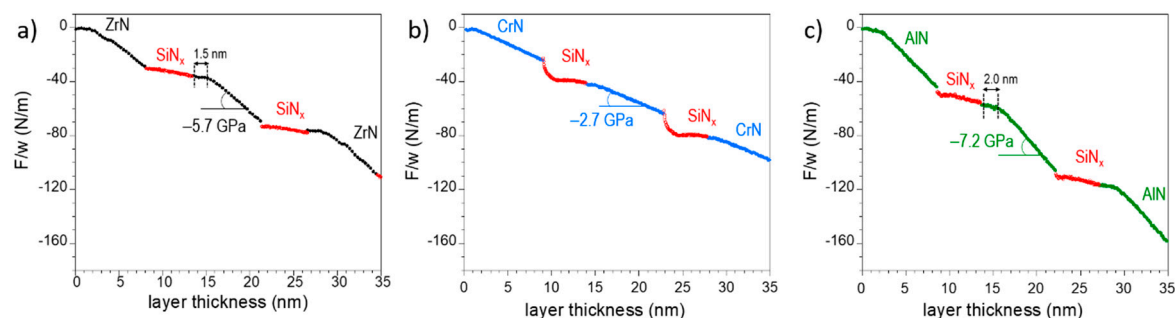

Figure 3. In situ stress evolution during growth of multilayered films: ZrN/SiN_x (**a**); CrN/SiN_x (**b**); and AlN/SiN_x (**c**). The data were obtained from MOSS and are displayed as the variation of the force per unit width (F/w) vs. layer thickness. The slope of the curves gives the information on the incremental stress, ranging from -7.2 GPa (AlN) to -2.7 GPa (CrN).

A closer inspection to the stress curves of Figure 3 reveals some interesting features. The development of compressive stress starts after ~1.5 nm and 2.0 nm for ZrN and AlN layers, respectively. Below these values, the stress is relatively small (about -1 GPa) and could reflect the initial formation of an amorphous layer. XRD characterizations on the MeN/SiN_x multilayers with 2 nm/5 nm thickness ratio support this scenario. Finally, it can be noticed in Figure 3b that the stress development during growth of SiN_x on CrN is peculiar, as a steady-state stress is only reached after ~2–3 nm. The larger compressive stress that develops in the very beginning is contributed to interface stress and possible interlayer formation, as also noticed from cross-section HRTEM view in Figure 1b.

In Figures 4–6 (see black lines for as-deposited state), the XRD patterns of reference monolithic ZrN (Figure 4a), CrN (Figure 5a) and AlN (Figure 6a) films are represented in comparison with the XRD patterns of MeN/SiN_x (Me = Zr, Cr, Al) multilayered films (Figure 4b–d, Figures 5b–d and 6b–d). The angular range 25–58° covers the main 111 and 200 Bragg reflections for cubic c-ZrN (JCPDS card

No. 35-0753), c-CrN (JCPDS card No. 76-2494) as well as 100, 002, 101 and 102 reflections for hexagonal h-AlN with wurtzite structure (JCPDS card No. 25-1133).
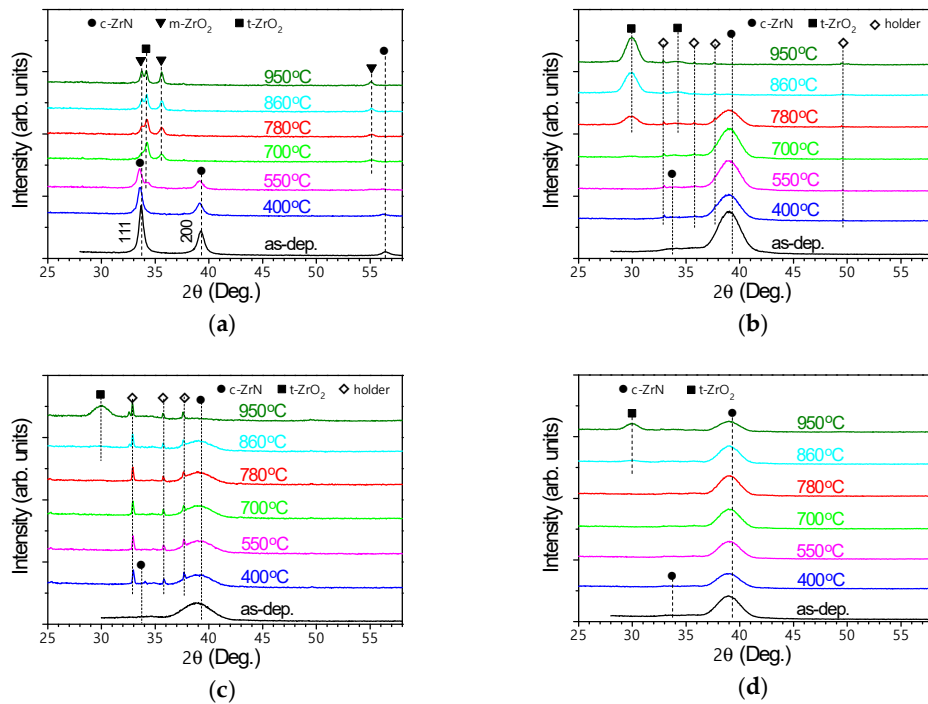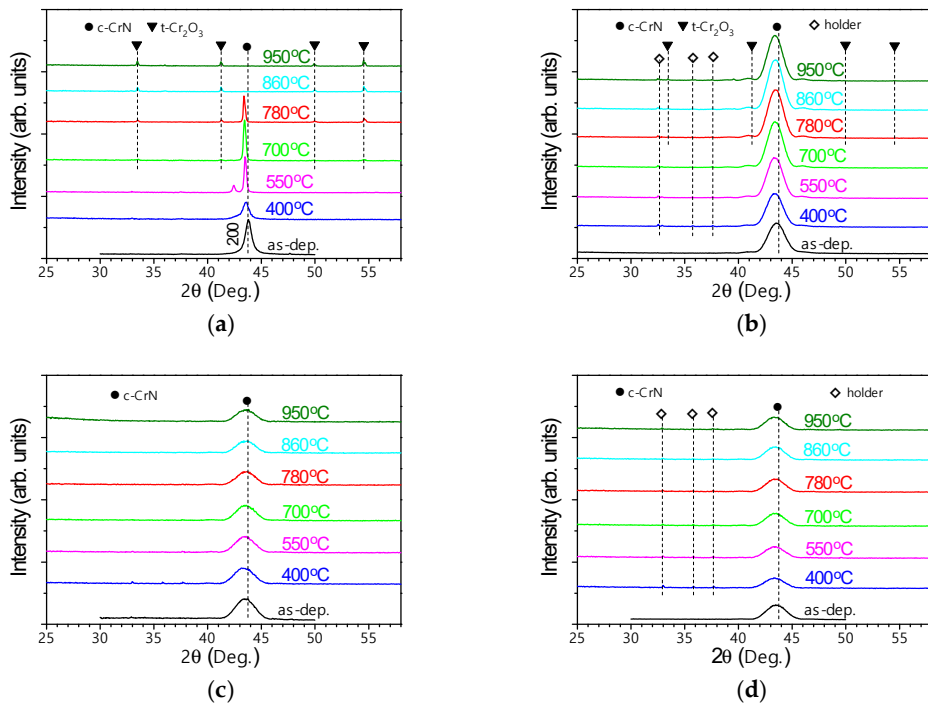

(a)

(b)

(c)

(d)

Figure 4. Evolution of XRD patterns under air annealing for ZrN reference film (**a**); and ZrN/SiN$_x$ multilayered films with different thickness of ZrN and SiN$_x$ elementary layers: (**b**) 5 nm/2 nm; (**c**) 5 nm/5 nm; and (**d**) 5 nm/10 nm.
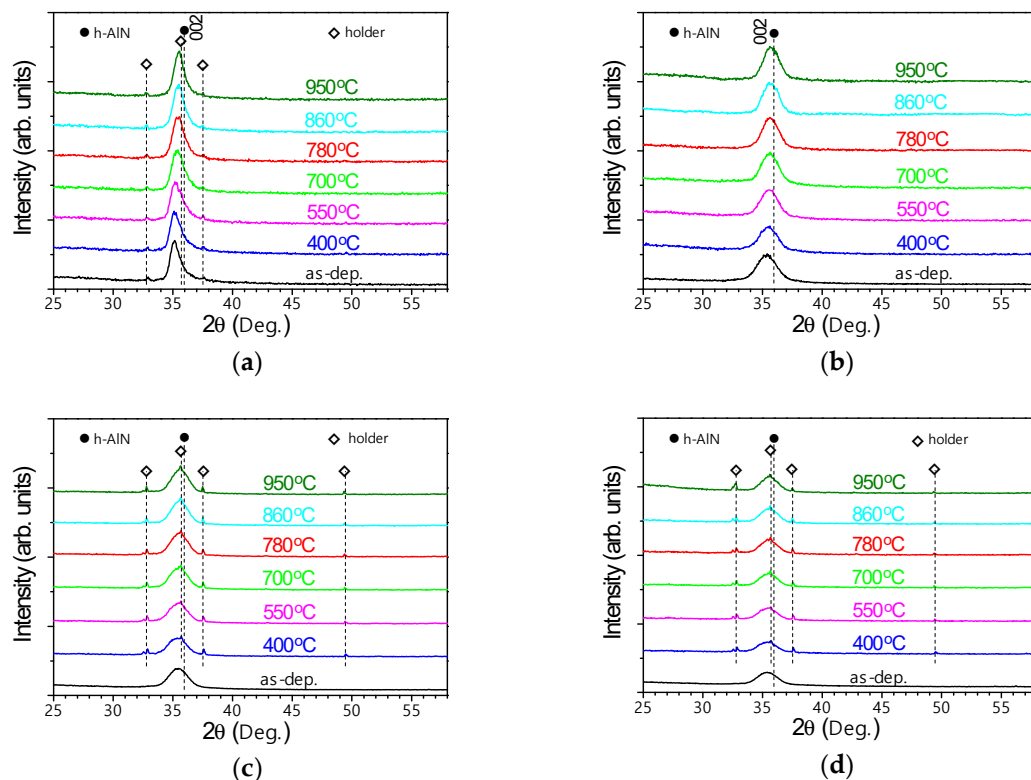

(a)

(b)

(c)

(d)

Figure 5. Evolution of XRD patterns under air annealing for CrN reference film (**a**); and CrN/SiN$_x$ multilayered films with different thickness of CrN and SiN$_x$ elementary layers: (**b**) 5 nm/2 nm; (**c**) 5 nm/5 nm; and (**d**) 5 nm/10 nm.

Figure 6. Evolution of XRD patterns under air annealing for AlN reference film (**a**); and AlN/SiN$_x$ multilayered films with different thickness of AlN and SiN$_x$ elementary layers: (**b**) 5 nm/2 nm; (**c**) 5 nm/5 nm; and (**d**) 5 nm/10 nm.

If for the reference c-ZrN film (Figure 4a) both (111) and (200) preferred orientations take place, in the case of reference c-CrN and h-AlN films, the preferred orientation along the [200] direction (c-CrN) or in the [002] direction (h-AlN) is only observed (Figures 5a and 6a). Competitive columnar growth between (111)- and (200)-oriented ZrN crystallites during sputter-deposition of ZrN monolithic films was discussed previously [23,35]. The (200) preferred orientation is characteristic for CrN films [39,40], as well as (002) preferred orientation is typical for h-AlN films [41–43]. Torino et al. [42] reported a transition from (101) to (002) preferred orientation for AlN films with decreasing (Ar + N$_2$) working pressure in the chamber. The presence of (002) orientation means that the AlN crystallites are highly oriented with the c-axis perpendicular to the substrate surface [43,44].

It was observed that the peak position of reference ZrN, CrN and AlN monolithic films is shifted to lower 2θ angles as compared to the position for bulk materials. This is related to the presence of in-plane compressive stresses, resulting in an expansion of the out-of-plane lattice parameter. For the AlN reference film, an asymmetry of the 002 peak towards higher 2θ angles was noticed, which can be due to a higher defect concentration. The reference Si$_3$N$_4$ film was found to be X-ray amorphous, i.e., there are no reflections in the investigated angular range (see [23]).

If we now analyze the XRD patterns of MeN/SiN$_x$ (Me = Zr, Cr, Al) multilayers in their as-deposited state, the following observations can be made in comparison with the reference MeN films: (i) a transition from (111) preferred orientation, which predominates for reference ZrN film (Figure 4a), to (200) orientation for ZrN/SiN$_x$ multilayered films (Figure 4b–d) and the retaining of (200) or (002) preferred orientation for CrN/SiN$_x$ (Figure 5b–d) or AlN/SiN$_x$ (Figure 6b–d) multilayered films as in the case of corresponding mononitrides CrN (Figure 5a) or AlN (Figure 6a); (ii) the broadening of the MeN XRD lines and decrease in their intensity that can be caused by the decrease in MeN crystallites size; and (iii) the amorphization of the MeN/SiN$_x$ (Me = Zr, Cr, Al) multilayered films when the MeN

layer thickness decreases down to 2 nm (XRD patterns of the ZrN/SiN$_x$ multilayer with 2 nm/5 nm thickness ratio can be found in our previous works [6,23]).

In the case of ZrN/SiN$_x$ multilayered films, the amorphous SiN$_x$ layer hinders the columnar growth of ZrN crystallites and favors the (200) preferred orientation [23]. The transition to (200) preferred orientation and broadening of ZrN peak with decreasing f_{MeN} was also observed by Dong et al. [25]. CrN/SiN$_x$ multilayered films were also characterized by (200) preferred orientation [20]. The present results allow concluding that the insertion of amorphous SiN$_x$ layers influence the structure of growing MeN layers.

As for the reference MeN$_x$ films, the position of ZrN and CrN 200 lines, and AlN 002 line is shifted to lower angles compared to position for bulk materials, in good agreement with an in-plane compressive stress state, as revealed from substrate curvature measurements (see Figure 3).

3.2. Evolution of Phase Composition of MeN/SiN$_x$ (Me = Zr, Cr, Al) Multilayered Films during Air Annealing

The evolution of XRD patterns for reference (monolithic) single-layer MeN and for multilayered films of different composition with the increase of air-annealing temperature from of 400 to 950 °C is shown in Figures 4–6. When considering the reference ZrN (Figure 4a), CrN (Figure 5a) and AlN (Figure 6a) films, it is worth noting the following. Oxidation of ZrN starts already at the temperature of 550 °C (t-ZrO$_2$ phase is registered), oxidation of CrN at the temperature of 700 °C (diffraction reflections of t-Cr$_2$O$_3$ phase appear), while the AlN film remains unaltered up to 950 °C. This shows the higher thermal stability of AlN. The peaks of ZrN and CrN phases disappear completely when reaching the temperature of 700 and 860 °C, respectively. It should be noted that the shoulder to the left from 200 c-CrN peak is detected for CrN film at the temperature of 400 °C, and afterwards the weak 111 reflection of h-Cr$_2$N phase (JCPDS card No. 35-0803) at $2\theta \approx 42.6°$ is registered at 550 °C (Figure 5a). Previous studies have also reported the transformation from c-CrN to h-Cr$_2$N phase during vacuum or air annealing [45,46] due to depletion in nitrogen. Both phases decompose with the formation of chromium oxides at the subsequent temperature rise.

In the case of ZrN/SiN$_x$ multilayered films (Figure 4b–d), the evolution of XRD patterns during air annealing depends on the f_{MeN} fraction. For ZrN/SiN$_x$ (5 nm/2 nm), for which $f_{MeN} > 0.50$, the crystallization of t-ZrO$_2$ oxide phase occurs at the temperatures of 700–780 °C (Figure 4b). When reaching the temperature of 860 °C, the 200 ZrN peak disappears, indicating the decomposition of the nitride phase and formation of zirconium oxides. For ZrN/SiN$_x$ (5 nm/5 nm) and ZrN/SiN$_x$ (5 nm/10 nm) films, for which $f_{MeN} < 0.50$ (Table 2), the crystallization of t-ZrO$_2$ takes place at the higher temperatures (860–950 °C). In the case of ZrN/SiN$_x$ (5 nm/10 nm), the ZrN peak remains until 950 °C (Figure 4d). Therefore, it can be concluded that oxidation resistance of ZrN/SiN$_x$ multilayers increases with increasing SiN$_x$ layer thickness from 2 to 10 nm at the constant thickness of 5 nm for ZrN layer. A similar trend of thermal stability enhancement with decreasing f_{MeN} fraction was reported earlier [6]. Note that the ZrN/SiN$_x$ (2 nm/5 nm) amorphous multilayer film was also stable in the temperature range of 400–950 °C, with no oxide phases detected (see Figure 13d in [6]). The value of f_{MeN} for this multilayer is similar to that for ZrN/SiN$_x$ (5 nm/10 nm) multilayer but the interface density is more than double (Table 2). This suggests that an increase in interface density also promotes the oxidation resistance of ZrN/SiN$_x$ multilayered films.

Contrarily to the reference CrN film (Figure 5a), CrN/SiN$_x$ multilayers were found to be thermally stable up to 950 °C. No crystalline oxide phases are detected up to temperature of 950 °C. For the CrN/SiN$_x$ (5 nm/2 nm) multilayered films (Figure 5b), the intensity of 200 CrN peak even slightly increases with temperature, which is most likely connected to some improvement of crystalline quality of this film. The CrN/SiN$_x$ (2 nm/5 nm) film, which was amorphous in its as-deposited state, remains amorphous after air annealing (not shown).

For the third multilayered system, i.e. for AlN/SiN$_x$ films, the emergence of oxide phases during air annealing is not registered for all studied thickness ratios of elementary layers, namely, 5 nm/2 nm, 5 nm/5 nm, 5 nm/10 nm and 2 nm/5 nm (Figure 6b–d). Intensity of 002 AlN peak rises slightly with the

increase in annealing temperature for all samples except for AlN/SiN$_x$ (2 nm/5 nm) film, which remains X-ray amorphous.

To get more insights on phase stability, we plot in Figure 7 the evolution of the out-of-plane lattice parameter of MeN layers with annealing temperature. Lattice parameter *a* of c-ZrN and c-CrN phases was calculated using angular position of 200 peak, and lattice parameter *c* of h-AlN phase using 002 peak. The results are shown for the reference ZrN, CrN and AlN films, as well as for MeN/SiN$_x$ (Me = Zr, Cr, Al) multilayers with 5 nm/5 nm and 5 nm/10 nm ratios. For AlN sub-layers, as well as AlN monolithic film, a substantial decrease of the lattice parameter was found, up to 0.7% relative reduction for the reference AlN film. This is contributed to the relaxation of compressive stress with increasing annealing temperature, which decreases propensity of film delamination and/or bucking and is therefore beneficial to its thermal stability. An opposite behavior was found for ZrN and CrN reference films, which could only be explained by decomposition of the MeN phase due to nitrogen release. For ZrN/SiN$_x$ and CrN/SiN$_x$ multilayers, one observes a competition between nitrogen loss and relaxation of compressive stress, depending on the annealing temperature.
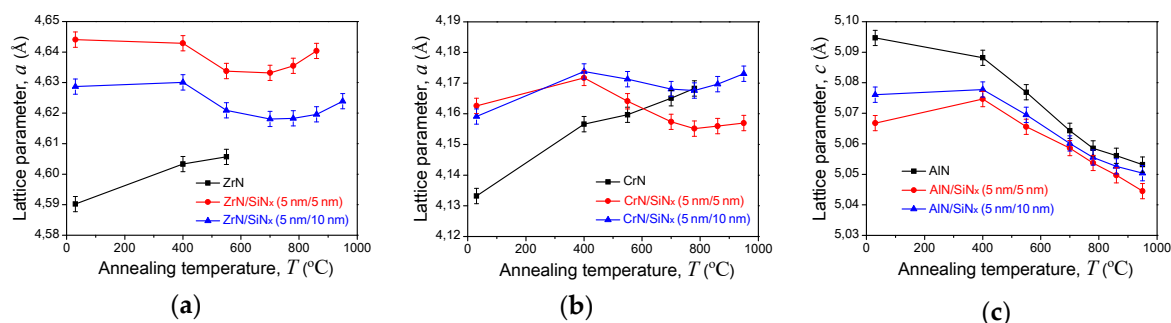

Figure 7. Dependences of the lattice parameter of MeN phase on the annealing temperature for multilayered films with comparison with the same dependences for reference monolithic films: ZrN/SiN$_x$ (**a**); CrN/SiN$_x$ (**b**); and AlN/SiN$_x$ (**c**).

3.3. Elemental Composition and Surface State of MeN/SiN$_x$ (Me = Zr, Cr, Al) Multilayered Films after Air Annealing Procedure

The composition of the reference ZrN, CrN, AlN and Si$_3$N$_4$ films as well as MeN/SiN$_x$ (Me = Zr, Cr, Al) multilayered films after air annealing up to 950 °C was measured by WDS. Concerning the multilayered films, it should be noted that by means of WDS the integral content of the elements (corresponding to the whole thickness of the coating) was determined. Consequently, the obtained data allowed carrying out the relative comparison of oxidation resistance of the multilayered films of three systems—ZrN/SiN$_x$, CrN/SiN$_x$ and AlN/SiN$_x$—with the same ratios of elementary layer thicknesses. The oxygen and nitrogen content in the film composition gives information on film stability after air-annealing. As the oxygen incorporates and substitutes the nitrogen atoms in MeN lattice during high-temperature annealing, the increase in oxygen content in the coating composition is always accompanied by a decrease in nitrogen content. The variation in oxygen content for the reference and multilayered films is displayed in Figure 8.

If the ZrN and CrN films are fully oxidized (the oxygen content is close to composition of ZrO$_2$ and Cr$_2$O$_3$ oxides, respectively), the AlN and Si$_3$N$_4$ films are characterized by a considerably lower degree of oxidation (around 30 at.%, see Figure 8). Overall, the MeN/SiN$_x$ multilayers show better oxidation resistance than their mononitride counterparts, in agreement with XRD analysis. For the ZrN/SiN$_x$ system, the tendency of oxidation resistance enhancement with decreasing f_{MeN} was clearly observed. In the case of CrN/SiN$_x$ and AlN/SiN$_x$ systems, the same tendency is revealed but it is much less pronounced. It is noteworthy that for CrN/SiN$_x$ and AlN/SiN$_x$ films the decrease in MeN layer thickness down to 2 nm leads to a certain deterioration of oxidation resistance.
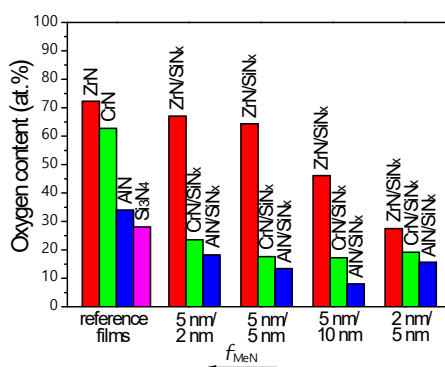
Figure 8. The oxygen content for the reference ZrN, CrN, AlN, and Si_3N_4 films as well as ZrN/SiN$_x$, CrN/SiN$_x$ and AlN/SiN$_x$ multilayered films with different ratios of the thicknesses of MeN and SiN$_x$ elementary layers after annealing in air at 950 °C.

The results reported in Figure 8 allow concluding that CrN/SiN$_x$ and AlN/SiN$_x$ multilayered films are significantly more stable under conditions of high-temperature annealing as compared to ZrN/SiN$_x$ films. These results agree with XRD data discussed in the previous section. The smallest content of oxygen (8 at. %) after annealing in air was registered for AlN/SiN$_x$ (5 nm/10 nm) film.

To clarify the mechanisms responsible for film oxidation, the analysis of the surface state was performed by SEM after high-temperature (950 °C) annealing. SEM observations reveal that the high degree of the coating damage, namely the emergence of corrosion sites, the swelling and flacking of the film, is inherent to the reference monolithic films, except for AlN surface, which remains quite uniform after annealing (see Figure 9).
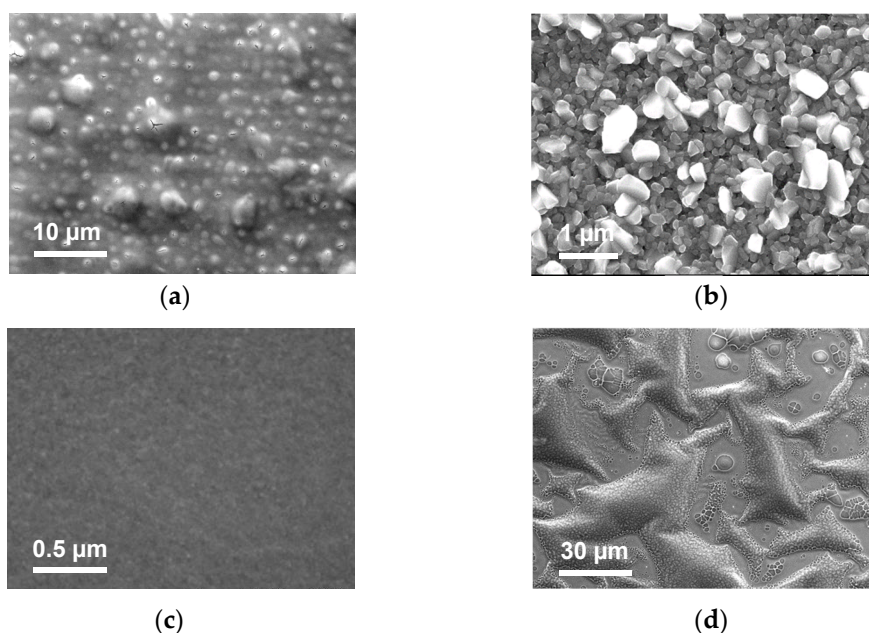

Figure 9. Top-view SEM micrographs of reference films after air annealing at 950 °C: ZrN (**a**); CrN (**b**); AlN (**c**); and Si_3N_4 (**d**). Note the different scale bar for the different images.

The MeN/SiN$_x$ (Me = Zr, Cr, Al) multilayered films are appreciably less subjected to surface damage after air annealing. Besides, the analysis of the surface topography of CrN/SiN$_x$ and AlN/SiN$_x$ multilayered films testifies to their lower susceptibility to oxidation compared to ZrN/SiN$_x$ films. As an example, the SEM micrographs of ZrN/SiN$_x$, CrN/SiN$_x$ and AlN/SiN$_x$ multilayered films with 5 nm/10 nm thickness ratio of elementary layers are represented in Figure 10. The lowest content of oxygen in

CrN/SiN$_x$ and AlN/SiN$_x$ films after air-annealing was revealed for such thickness ratio (Figure 8). Large corroded areas were observed on the surface of ZrN/SiN$_x$ coating (Figure 10a), while the surface of the CrN/SiN$_x$ coating is characterized by the presence of much smaller defects, which, however, do not cause any failure of the coating integrity (Figure 10b). The surface relief of the AlN/SiN$_x$ film is rather uniform (Figure 10c). Shallow, nanoscale blisters are only visible, with no sign of localized oxidation. These observations confirm the better oxidation resistance of AlN/SiN$_x$ multilayers, comparatively to CrN/SiN$_x$ and ZrN/SiN$_x$ systems.

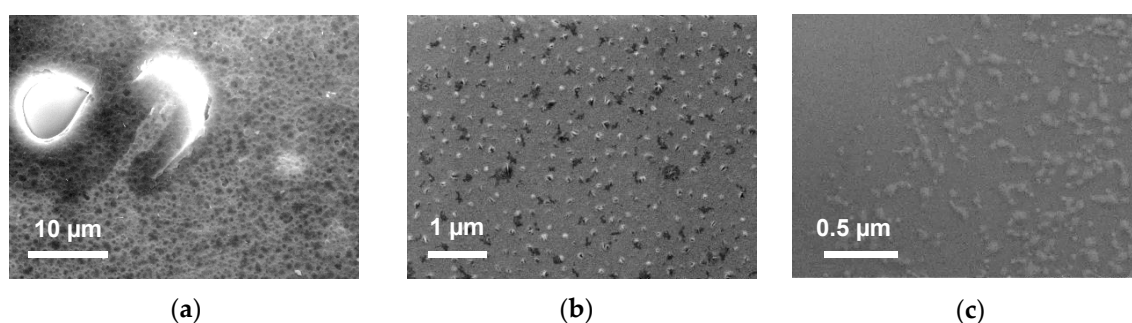**(a)**　　　　　　　　　　　**(b)**　　　　　　　　　　　**(c)**

Figure 10. Top-view SEM micrographs of multilayered films with the ratio of thicknesses of MeN and SiN$_x$ elementary layers equal to 5 nm/10 nm after air annealing at 950 °C: ZrN/SiN$_x$ (**a**); CrN/SiN$_x$ (**b**); and AlN/SiN$_x$ (**c**). Note the different scale bar for the different images.

3.4. Discussion on the Comparative Oxidation Resistance of MeN/SiN$_x$ Multilayers and Me-Si-N Single-Layers

As pointed out in the Introduction, there exists two approaches for the synthesis of hard TMN coatings with enhanced phase stability during high-temperature air annealing, namely the formation of nanocomposite/amorphous Me-Si-N films or MeN/SiN$_x$ multilayered films. Therefore, it is rather interesting to compare their oxidation resistance. In general, the thermal stability of MeN$_x$ phase is determined by its decomposition into Me and N$_2$(g), which depends on the stoichiometry x = [N]/[Me]. In Zr-Si-N amorphous films, a worse thermal stability was reported for films with substoichiometric ZrN$_{x<1}$ phase [8]. Similar conclusions can also be made from the work of Abadias et al. on quaternary TiZrAl$_x$N$_y$ films [47]. However, the resistance to oxidation during air annealing of MeN$_x$ phase is also determined by its ability for crystallization of metal oxide (MeO$_x$) phases and the type of MeO$_x$ formed (dense solid vs. volatile oxides or passivating oxides) that impact coating morphology [4,9]. The present findings show that, despite CrN layers being substoichiometric (see Table 1), the oxidation resistance of CrN/SiN$_x$ multilayers (at least up to 950 °C) is higher than that of ZrN/SiN$_x$ multilayers (up to 860 °C).

Numerous works have been dedicated to study the oxidation behavior of Me-Si-N systems, including Zr-Si-N [7–10,48,49], W-Si-N [8–10], Ta-Si-N [8–10,50], Cr-Si-N [51], or Al-Si-N [8–10,52]. With increasing Si fraction, the microstructure typically evolves from bi-phase nanocomposites consisting of MeN$_x$ nanocrystals embedded in Si$_3$N$_4$ amorphous phase to X-ray amorphous phase. As an example, for Zr-Si-N coatings, the oxidation resistance rises with the increase of Si content, i.e. with increasing volume fraction of amorphous Si$_3$N$_4$ phase [6,48,49]. The best oxidation resistance is achieved for amorphous coatings, typically exceeding 1000 °C under air [9,52]. In the case of the Zr-Si-N system, the absence of mass gain was observed even up to the temperature of 1300 °C [9].

In a previous study [6], we compared the oxidation resistance of ZrSiN nanocomposite and ZrN/SiN$_x$ multilayered films. It should be pointed that the investigated films were relatively thin (thickness of ~300 nm) that resulted in a significant fraction of the oxidized layer. When using the same deposition conditions, the oxidation starts at 700–780 °C for ZrSiN nanocomposite films and at 860–950 °C for ZrN/SiN$_x$ multilayered films. This testifies to the advantage of the multilayered films. The lower degree of the compressive stress relaxation at the elevated temperatures of ZrSiN films, as compared to ZrN/SiN$_x$ multilayered films, was likely at the origin of film cracking, which

deteriorates their oxidation resistance. The formation of cracks was indeed observed for nanocomposite and amorphous ZrSiN films despite reduction in oxygen penetration into the film with increasing Si content [6]. However, no cracks were observed for the ZrN/SiN_x multilayers.

4. Summary and Conclusions

By means of magnetron sputter deposition technique, single-layer (monolithic) ZrN, CrN, AlN and Si_3N_4 films and MeN/SiN_x (Me = Zr, Cr, Al) multilayered films with the different ratios of MeN layer thickness to SiN_x layer thickness, namely 5 nm/2 nm, 5 nm/5 nm, 5 nm/10 nm and 2 nm/5 nm, were synthesized. The structure and phase composition of the films in as-deposited state as well as their stability under air-annealing in the 400–950 °C temperature range were studied.

TEM, XRR and XRD results disclose the formation of periodic MeN/SiN_x multilayered structures characterized by uniform alternation of nanocrystalline MeN layers and amorphous SiN_x layers with sharp and planar interfaces. In the case of ZrN/SiN_x and CrN/SiN_x systems, the MeN phase has (200) preferred orientation of the crystallites. In the case of AlN/SiN_x film, the (002) preferred orientation was observed. For all multilayered films, the decrease in crystallites size of MeN phase occurs, and this phase becomes X-ray amorphous (as well as SiN_x phase) when reducing the thickness of the corresponding elementary layer down to 2 nm.

The results of XRD, WDS and SEM analysis point that all reference monolithic films are subjected to significant oxidation level during high-temperature annealing. ZrN oxidizes into $t-ZrO_2$ at 550 °C, while CrN first decomposes into Cr_2N at 550 °C, followed by the formation of $t-Cr_2O_3$ phase at 700 °C. AlN and Si_3N_4 films appear more thermally stable, with lower oxygen uptake at 950 °C and no crystalline oxides detected. Compared to MeN single-layers, MeN/SiN_x multilayers exhibit improved oxidation resistance due to the presence of amorphous Si_3N_4 layers: ZrN/SiN_x multilayers start to oxidize at the temperatures of 780–860 °C, while CrN/SiN_x and AlN/SiN_x multilayered films are stable up to 950 °C. Further investigations at higher temperatures would be required to assess the upper temperature limit of their stability in air, and evaluate their performance comparatively to amorphous ternary Me-Si-N films, which are thermally stable and oxidation resistant up to ~1300 °C [9].

For ZrN/SiN_x multilayered films, both the reduction of f_{MeN} fraction and increase in number of the bilayers in the film improve their oxidation resistance. However, ZrN/SiN_x multilayered films are least thermally stable among the three studied systems. The minimum oxygen content (27.5 at. %) after air annealing is found for the ZrN/SiN_x (2 nm/5 nm) film.

The CrN/SiN_x and AlN/SiN_x multilayered films are characterized by appreciably higher stability of their phase composition during air annealing. The oxygen content after annealing is in the 17.2–23.5 at.% (CrN/SiN_x films) and 8.0–18.2 at.% (AlN/SiN_x films) range. Both the passivating role of the chromium (or, especially, aluminum) oxides and the decrease in the compressive stresses during annealing (stress relaxation) are apparently the main reasons for the improvement of film properties. In contrast to ZrN/SiN_x films, for CrN/SiN_x and AlN/SiN_x multilayered films, the decrease in MeN layer thickness down to 2 nm leads to certain deterioration of their oxidation resistance. This can be connected to the fact that the passivating role of the chromium or aluminum oxides in the surface layers of multilayered film is less effective at such a small thickness of elementary layer.

The CrN/SiN_x and AlN/SiN_x multilayered films with the thickness ratios of elementary layers of 5 nm/5 nm and 5 nm/10 nm are the most promising for practical applications at elevated temperatures (up to 950 °C). The absence of the explicit corrosion sites on the surface is evidenced for AlN/SiN_x films. Among the studied samples, the lowest oxidation level was obtained for the AlN/SiN_x (5 nm/10 nm) multilayer, for which the oxygen content after air annealing is only 8.0 at.%.

Conflicts of Interest: The authors declare no conflict of interest. The funders had no role in the design of the study; in the collection, analyses, or interpretation of data; in the writing of the manuscript, or in the decision to publish the results.

References

1. Milosev, I.; Strehblow, H.-H.; Navinsek, B. Comparison of TiN, ZrN and CrN hard nitride coatings: Electrochemical and thermal oxidation. *Thin Solid Films* **1997**, *303*, 246–254. [CrossRef]
2. Vaz, F.; Ferreira, J.; Ribeiro, E.; Rebouta, L.; Lanceros-Mendez, S.; Mendes, J.A.; Alves, E.; Goudeau, P.; Riviere, J.P.; Ribeiro, F.; et al. Influence of nitrogen content on the structural, mechanical and electrical properties of TiN thin films. *Surf. Coat. Technol.* **2005**, *191*, 317–323. [CrossRef]
3. Wen, F.; Meng, Y.D.; Ren, Z.X.; Shu, X.S. Microstructure, hardness and corrosion resistance of ZrN films prepared by inductively coupled plasma enhanced RF magnetron sputtering. *Plasma Sci. Technol.* **2008**, *10*, 170–175. [CrossRef]
4. Abadias, G.; Koutsokeras, L.E.; Siozios, A.; Patsalas, P. Stress, phase stability and oxidation resistance of ternary Ti–Me–N (Me = Zr, Ta) hard coatings. *Thin Solid Films* **2013**, *538*, 56–70. [CrossRef]
5. Barshilia, H.C.; Deepthi, B.; Arun Prabhu, A.S.; Rajam, K.S. Superhard nanocomposite coatings of TiN/Si$_3$N prepared by reactive direct current unbalanced magnetron sputtering. *Surf. Coat. Technol.* **2006**, *201*, 329–337. [CrossRef]
6. Saladukhin, I.A.; Abadias, G.; Uglov, V.V.; Zlotski, S.V.; Michel, A.; Vuuren, A.J. Thermal stability and oxidation resistance of ZrSiN nanocomposite and ZrN/SiN$_x$ multilayered coatings: A comparative study. *Surf. Coat. Technol.* **2017**, *332*, 428–439. [CrossRef]
7. Silva Neto, P.C.; Freitas, F.G.R.; Fernandez, D.A.R.; Carvalho, R.G.; Felix, L.C.; Tertoa, A.R.; Hubler, R.; Mendes, F.M.T.; Silva Junior, A.H.; Tentardini, E.K. Investigation of microstructure and properties of magnetron sputtered Zr-Si-N thin films with different Si content. *Surf. Coat. Technol.* **2018**, *353*, 355–363. [CrossRef]
8. Musil, J.; Vlček, J.; Zeman, P. Hard amorphous nanocomposite coatings with oxidation resistance above 1000 °C. *Adv. Appl. Ceram.* **2008**, *107*, 148–154. [CrossRef]
9. Musil, J. Hard nanocomposite coatings: Thermal stability, oxidation resistance and toughness. *Surf. Coat. Technol.* **2012**, *207*, 50–65. [CrossRef]
10. Musil, J. Advanced Hard Nanocoatings: Present State and Trends. In *Top 5 Contributions in Molecular Sciences*, 6th ed.; Avid Science; Telanga India: Berlin, Germany, 2020; pp. 2–65.
11. Abadias, G.; Michel, A.; Tromas, C.; Jaouen, C.; Dub, S.N. Stress, interfacial effects and mechanical properties of nanoscale multilayered coatings. *Surf. Coat. Technol.* **2007**, *202*, 844–853. [CrossRef]
12. Bobzin, K.; Brögelmann, T.; Kruppe, N.C.; Arghavani, M.; Mayer, J.; Weirich, T.E. Plastic deformation behavior of nanostructured CrN/AlN multilayer coatings deposited by hybrid dcMS/HPPMS. *Surf. Coat. Technol.* **2017**, *332*, 253–261. [CrossRef]
13. Chang, Y.-Y.; Weng, S.-Y.; Chen, C.-H.; Fu, F.-X. High temperature oxidation and cutting performance of AlCrN, TiVN and multilayered AlCrN/TiVN hard coatings. *Surf. Coat. Technol.* **2017**, *332*, 494–503. [CrossRef]
14. Contreras, E.; Galindez, Y.; Rodas, M.A.; Bejarano, G.; Gómez, M.A. CrVN/TiN nanoscale multilayer coatings deposited by DC unbalanced magnetron sputtering. *Surf. Coat. Technol.* **2017**, *332*, 214–222. [CrossRef]
15. Pogrebnjak, A.; Smyrnova, K.; Bondar, O. Nanocomposite Multilayer Binary Nitride Coatings Based on Transition and Refractory Metals: Structure and Properties. *Coatings* **2019**, *9*, 155. [CrossRef]
16. Lei, Z.; Liu, Y.; Ma, F.; Song, Z.; Li, Y. Oxidation resistance of TiAlN/ZrN multilayer coatings. *Vacuum* **2016**, *127*, 22–29. [CrossRef]
17. Xiao, B.; Li, H.; Mei, H.; Dai, W.; Zuo, F.; Wu, Z.; Wang, Q. A study of oxidation behavior of AlTiN-and AlCrN-based multilayer coatings. *Surf. Coat. Technol.* **2018**, *333*, 229–237. [CrossRef]
18. Kong, M.; Zhao, W.; Wei, L.; Li, G. Investigations on the microstructure and hardening mechanism of TiN/Si$_3$N$_4$ nanocomposite coatings. *J. Phys. D Appl. Phys.* **2007**, *40*, 2858. [CrossRef]

19. Wu, Z.; Zhong, X.; Liu, C.; Wang, Z.; Dai, W.; Wang, Q. Plastic Deformation Induced by Nanoindentation Test Applied on ZrN/Si$_3$N$_4$ Multilayer Coatings. *Coatings* **2018**, *8*, 11. [CrossRef]

20. Bai, X.; Zheng, W.; An, T.; Jiang, Q. Effects of deposition parameters on microstructure of CrN/Si$_3$N$_4$ nanolayered coatings and their thermal stability. *J. Phys. Condens. Matter* **2005**, *17*, 6405–6413. [CrossRef]

21. Soares, T.P.; Aguzzoli, C.; Soares, G.V.; Figueroa, C.A.; Baumvol, I.J.R. Physicochemical and mechanical properties of crystalline/amorphous CrN/Si$_3$N$_4$ multilayers. *Surf. Coat. Technol.* **2013**, *237*, 170–175. [CrossRef]

22. Hultman, L.; Bareño, J.; Flink, A.; Söderberg, H.; Larsson, K.; Petrova, V.; Odén, M.; Greene, J.E.; Petrov, I. Interface structure in superhard TiN-SiN nanolaminates and nanocomposites: Film growth experiments and ab initio calculations. *Phys. Rev. B* **2007**, *75*, 155437. [CrossRef]

23. Abadias, G.; Uglov, V.V.; Saladukhin, I.A.; Zlotski, S.V.; Tolmachova, G.; Dub, S.N.; Vuuren, A.J. Growth, structural and mechanical properties of magnetron-sputtered ZrN/SiN$_x$ nanolaminated coatings. *Surf. Coat. Technol.* **2016**, *308*, 158–167. [CrossRef]

24. Söderberg, H.; Odén, M.; Larsson, T.; Hultman, L.; Molina-Adareguia, J.M. Epitaxial stabilization of cubic-SiN$_x$ in TiN/SiN$_x$ multilayers. *Appl. Phys. Lett.* **2006**, *88*, 191902. [CrossRef]

25. Dong, Y.; Zhao, W.; Yue, J.; Li, G. Crystallization of Si$_3$N$_4$ layers and its influences on the microstructure and mechanical properties of ZrN/Si$_3$N$_4$ nanomultilayers. *Appl. Phys. Lett.* **2006**, *89*, 121916. [CrossRef]

26. Ghafoor, N.; Lind, H.; Tasnar̓di, F.; Abrikosov, I.A.; Oder̓n, M. Anomalous epitaxial stability of (001) interfaces in ZrN/SiN$_x$ multilayers. *APL Mater.* **2014**, *2*, 046106. [CrossRef]

27. Parlinska-Wojtan, M.; Pélisson-Schecker, A.; Hug, H.J.; Rutkowski, B.; Patscheider, J. AlN/Si$_3$N$_4$ multilayers as an interface model system for Al$_{1-x}$Si$_x$N/Si$_3$N$_4$ nanocomposite thin films. *Surf. Coat. Technol.* **2015**, *261*, 418–425. [CrossRef]

28. Huang, L.; Chen, Z.Q.; Liu, W.B.; Huang, P.; Meng, X.K.; Xu, K.W.; Wang, F.; Lu, T.J. Enhanced irradiation resistance of amorphous alloys by introducing amorphous/amorphous interfaces. *Intermetallics* **2019**, *107*, 39–46. [CrossRef]

29. Mège-Revil, A.; Steyer, P.; Cardinal, S.; Thollet, G.; Esnouf, C.; Jacquot, P.; Stauder, B. Correlation between thermal fatigue and thermomechanical properties during the oxidation of multilayered TiSiN nanocomposite coatings synthesized by a hybrid physical/chemical vapour deposition process. *Thin Solid Films* **2010**, *518*, 5932–5937. [CrossRef]

30. Colin, J.J.; Diot, Y.; Guerin, P.; Lamongie, B.; Berneau, F.; Michel, A.; Jaouen, C.; Abadias, G. A load-lock compatible system for in situ electrical resistivity measurements during thin film growth. *Rev. Sci. Instrum.* **2016**, *87*, 023902. [CrossRef]

31. Abadias, G.; Koutsokeras, L.E.; Dub, S.N.; Tolmachova, G.N.; Debelle, A.; Sauvage, T.; Villechaise, P. Reactive magnetron cosputtering of hard and conductive ternary nitride thin films: Ti–Zr–N and Ti–Ta–N. *J. Vac. Sci. Technol. A* **2010**, *28*, 541–551. [CrossRef]

32. Simonot, L.; Babonneau, D.; Camelio, S.; Lantiat, D.; Guérin, P.; Lamongie, B.; Antad, V. In situ optical spectroscopy during deposition of Ag:Si$_3$N$_4$ nanocomposite films by magnetron sputtering. *Thin Solid Films* **2010**, *518*, 2637–2643. [CrossRef]

33. Abadias, G.; Chason, E.; Keckes, J.; Sebastiani, M.; Thompson, G.B.; Barthel, E.; Doll, G.L.; Murray, C.E.; Stoessel, C.H.; Martinu, L. Review Article: Stress in thin films and coatings: Current status, hallenges, and prospects. *J. Vac. Sci. Technol. A* **2018**, *36*, 20801. [CrossRef]

34. Parratt, L.G. Surface Studies of Solids by Total Reflection of X-Rays. *Phys. Rev.* **1954**, *95*, 359–369. [CrossRef]

35. Koutsokeras, L.E.; Abadias, G. Intrinsic stress in ZrN thin films: Evaluation of grain boundary contribution from in situ wafer curvature and ex situ X-ray diffraction techniques. *J. Appl. Phys.* **2012**, *111*, 093509. [CrossRef]

36. Abadias, G.; Ivashchenko, V.I.; Belliard, L.; Djemia, P. Structure, phase stability and elastic properties in the Ti$_{1-x}$Zr$_x$N thin-film system: Experimental and computational studies. *Acta Mater.* **2012**, *60*, 5601–5614. [CrossRef]

37. Patsalas, P.; Kalfagiannis, N.; Kassavetis, S.; Abadias, G.; Bellas, R.V.; Lekka, C.; Lidorikis, E. Conductive nitrides: Growth principles, optical and electronic properties, and their perspectives in photonics and plasmonics. *Mater. Sci. Eng. R* **2018**, *123*, 1–55. [CrossRef]

38. Musil, J. Flexible Hard Nanocomposite Coatings. *RSC Adv.* **2015**, *5*, 60482–60495. [CrossRef]

39. Xingrun, R.; Zhu, H.; Meixia, L.; Jiangao, Y.; Hao, C. Comparison of microstructure and tribological behaviors of CrAlN and CrN film deposited by DC magnetron sputtering. *Rare Met. Mater. Eng.* **2018**, *47*, 1100–1106. [CrossRef]

40. Ren, X.; Zhang, Q.; Huang, X.; Su, W.; Yang, J.; Chen, H. Microstructure and tribological properties of CrN films deposited by direct current magnetron sputtering. *Rare Met. Mater. Eng.* **2018**, *47*, 2283–2289. [CrossRef]

41. Khan, S.; Shahid, M.; Mahmood, A.; Shah, A.; Ahmed, I.; Mehmood, M.; Aziz, U.; Raza, Q.; Alam, M. Texture of the nano-crystalline AlN thin films and the growth conditions in DC magnetron sputtering. *Prog. Nat. Sci. Mater. Int.* **2015**, *25*, 282–290. [CrossRef]

42. Taurino, A.; Signore, M.A.; Catalano, M.; Kim, M.J. (101) and (002) oriented AlN thin films deposited by sputtering. *Mater. Lett.* **2017**, *200*, 18–20. [CrossRef]

43. Signore, M.A.; Taurino, A.; Valerini, D.; Rizzo, A.; Farella, I.; Catalano, M.; Quaranta, F.; Siciliano, P. Role of oxygen contaminant on the physical properties of sputtered AlN thin films. *J. Alloys Compd.* **2015**, *649*, 1267–1272. [CrossRef]

44. Riah, B.; Ayad, A.; Camus, J.; Rammal, M.; Boukari, F.; Chekour, L.; Djouadi, M.A.; Rouag, N. Textured hexagonal and cubic phases of AlN films deposited on Si (100) by DC magnetron sputtering and high power impulse magnetron sputtering. *Thin Solid Films* **2018**, *655*, 34–40. [CrossRef]

45. Mayrhofer, P.H.; Rovere, F.; Moser, M.; Strondl, C.; Tietema, R. Thermally induced transitions of CrN thin films. *Scr. Mater.* **2007**, *57*, 249–252. [CrossRef]

46. Lin, J.; Moore, J.J.; Wang, J.; Sproul, W.D. High temperature oxidation behavior of CrN/AlN superlattice films. *Thin Solid Films* **2011**, *519*, 2402–2408. [CrossRef]

47. Abadias, G.; Saladukhin, I.A.; Uglov, V.V.; Zlotski, S.V.; Eyidi, D. Thermal stability and oxidation behavior of quaternary TiZrAlN magnetron sputtered thin films: Influence of the pristine microstructure. *Surf. Coat. Technol.* **2013**, *237*, 187–195. [CrossRef]

48. Pilloud, D.; Pierson, J.F.; Marco de Lucas, M.C.; Alnot, M. Stabilisation of tetragonal zirconia in oxidized Zr–Si–N nanocomposite coatings. *Appl. Surf. Sci.* **2004**, *229*, 132–139. [CrossRef]

49. Chen, Y.-I.; Chang, S.-C.; Chang, L.-C. Oxidation resistance and mechanical properties of Zr–Si–N coatings with cyclic gradient concentration. *Surf. Coat. Technol.* **2017**, *320*, 168–173. [CrossRef]

50. Chen, Y.-I.; Gao, Y.-X.; Chang, L.-C. Oxidation behavior of Ta-Si-N coatings. *Surf. Coat. Technol.* **2017**, *332*, 72–79. [CrossRef]

51. Mikula, M.; Grančič, B.; Drienovský, M.; Satrapinskyy, L.; Roch, T.; Hájovská, Z.; Gregor, M.; Plecenik, T.; Čička, R.; Plecenik, A.; et al. Thermal stability and high-temperature oxidation behavior of Si–Cr–N coatings with high content of silicon. *Surf. Coat. Technol.* **2013**, *232*, 349–356. [CrossRef]

52. Musil, J.; Remnev, G.; Legostaev, V.; Uglov, V.; Lebedynskiy, A.; Lauk, A.; Procházka, J.; Haviar, S.; Smolyanskiy, E. Flexible hard Al-Si-N films for high temperature operation. *Surf. Coat. Technol.* **2016**, *307*, 1112–1118. [CrossRef]